



**Sb<sub>2</sub>Se<sub>3</sub>(100): A strongly anisotropic surface**Roberta Totani <sup>1</sup>, Fabian O. von Rohr,<sup>1,2</sup> Jianzhou Zhao,<sup>1,3</sup> Zbynek Novotny,<sup>1,4</sup> Wolf-Dietrich Zabka,<sup>1</sup> Alexey Soluyanov,<sup>1,5</sup> and Jürg Osterwalder <sup>1,\*</sup><sup>1</sup>*Department of Physics, University of Zürich, Winterthurerstrasse 190, CH-8057 Zürich, Switzerland*<sup>2</sup>*Department of Chemistry, University of Zürich, Winterthurerstrasse 190, CH-8057 Zürich, Switzerland*<sup>3</sup>*Co-Innovation Center for New Energetic Materials, Southwest University of Science and Technology, Mianyang, Sichuan 621010, China*<sup>4</sup>*Paul Scherrer Institut, Forschungsstrasse 111, CH-5232 Villigen-PSI, Switzerland*<sup>5</sup>*Department of Physics, St. Petersburg State University, 199034 Russia*

(Received 21 September 2019; published 19 December 2019)

Interest in antimony selenide (Sb<sub>2</sub>Se<sub>3</sub>) has been constantly growing in the recent past, especially for its promising properties for applications in the field of solar energy technologies. Surprisingly, the surface properties of this material, which is built from van der Waals stacked one-dimensional (1D) ribbons, have not been studied in detail yet. Here we demonstrate that Sb<sub>2</sub>Se<sub>3</sub> crystals cleave along the (100) planes. The resulting surface shows a pronounced 1D structure, reflecting the stacking of ribbons in the bulk crystal. The cleaving process leads to the formation of slightly tilted surface domains, with the tilt angles oriented invariably along the ribbon directions, suggesting a strong anisotropy of the internal friction forces. Our angle-resolved photoemission data reveal that the 1D character of the crystalline structure of this material is also reflected in its electronic band structure.

DOI: [10.1103/PhysRevMaterials.3.125404](https://doi.org/10.1103/PhysRevMaterials.3.125404)**I. INTRODUCTION**

Antimony selenide (Sb<sub>2</sub>Se<sub>3</sub>) is a semiconductor from the binary V<sub>2</sub>-VI<sub>3</sub> compound family. In contrast with other members of this family, e.g., Bi<sub>2</sub>Se<sub>3</sub>, Bi<sub>2</sub>Te<sub>3</sub>, and Sb<sub>2</sub>Te<sub>3</sub>, the band structure of Sb<sub>2</sub>Se<sub>3</sub> is topologically trivial [1], hence this compound has not been in the recent focus of the condensed-matter physics community. Nonetheless, it has been widely investigated since the 1960s because of its anisotropic structure, which is responsible for intriguing anisotropic optical and transport properties [2,3]. Furthermore, this material has shown promising potential for various applications in several fields: together with other selenides and tellurides as a high-performance thermoelectric [4–6], as a pristine material for memory switching [7], and in its amorphous form for optical storage [8]. However, it is in the field of solar energy technologies, photovoltaics, and photocatalysis in particular, that Sb<sub>2</sub>Se<sub>3</sub> currently finds increased attention. In fact, its constituents are earth-abundant, have low toxicity, and are of relatively low cost [9]. It is a binary chalcogenide, allowing a much simpler control over its phase and defects, with respect to other multinary chalcogenides [10]. It has a very convenient direct band gap of 1.2 eV, with a high optical absorption coefficient [9,11]. The crystal structure of Sb<sub>2</sub>Se<sub>3</sub> is formed by covalently bonded ribbons, whose edges are occupied by saturated atoms, minimizing recombination losses [12]. These properties assure efficiency in visible-to-infrared light absorption and in subsequent electron-hole separation. For these reasons, Sb<sub>2</sub>Se<sub>3</sub> thin films started to be employed in solar cell devices [13]. More recently, the photocatalysis community has also developed a certain interest in this material, thanks to its

resistance to photocorrosion in an aqueous environment and because its conduction-band minimum is located at  $-4.15$  eV [14] with respect to the vacuum level, which is very suitable for the hydrogen evolution reaction. Sb<sub>2</sub>Se<sub>3</sub> thin films and nanostructures, implemented in photoelectrochemical cells, show promising performance in terms of photocurrent and stability [14–17].

Sb<sub>2</sub>Se<sub>3</sub> crystallizes in the Sb<sub>2</sub>S<sub>3</sub>-type structure, also known as the stibnite structure, referring to the naturally occurring mineral with the same name. It has an orthorhombic unit cell containing four Sb<sub>2</sub>Se<sub>3</sub> subunits [18] [Fig. 1(a)]. Its crystal structure is highly anisotropic, with one-dimensional (1D) ribbons formed by [Sb<sub>4</sub>Se<sub>6</sub>]<sub>n</sub> units extending infinitely along the [010] direction. While strong covalent bonds act within these units, only weak van der Waals forces connect neighboring ribbons. The distinctive staggering of the ribbons leads to a well-defined layered structure, with cleavage planes that are easily recognizable, as evidenced by the dashed “zig-zag” lines in Fig. 1(a).

Encouraged by the recent growing interest in this material and intrigued by the peculiar nature of the cleavage planes, we have studied the structural and electronic properties of freshly cleaved Sb<sub>2</sub>Se<sub>3</sub> single crystal surfaces. X-ray photoelectron spectroscopy (XPS) proved the effectiveness of cleaving to obtain atomically clean surfaces. Low-energy electron diffraction (LEED), atomic force microscopy (AFM), scanning tunneling microscopy (STM), and x-ray photoelectron diffraction (XPD) confirmed that the crystals cleave along (100) planes, exposing parallel edges of [Sb<sub>4</sub>Se<sub>6</sub>]<sub>n</sub> ribbons along the [010] direction that give the surface a marked 1D appearance. Important information about the surface morphology was also extracted by using these techniques, discovering the existence of non-ideal features along the ribbon direction. The band structure measured

\*osterwal@physik.uzh.ch

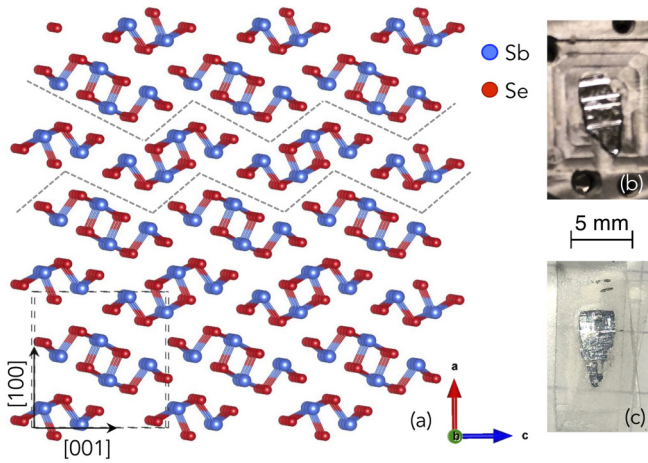


FIG. 1. (a) Crystalline structure displaying the (010) plane. Dashed lines evince the unit cell. “Zig-zag” dashed lines indicate the cleavage planes. (b)  $\text{Sb}_2\text{Se}_3$  single crystal mounted on a sample holder. (c)  $\text{Sb}_2\text{Se}_3$  remaining on the scotch tape after cleavage.

with angle-resolved photoemission spectroscopy (ARPES) and calculated with density functional theory (DFT) reflects the strongly anisotropic character and shows much stronger dispersion along the ribbons than across them. This study establishes the surface properties of a clean  $\text{Sb}_2\text{Se}_3(100)$  surface and serves as a basis for the investigation of heterostructures and interfaces involving this material, such as those found, e.g., in photovoltaics and photoelectrochemical cells.

## II. EXPERIMENTAL DETAILS

Large  $\sim 10 \times 4 \times 4 \text{ mm}^3$  single crystals of  $\text{Sb}_2\text{Se}_3$  were grown by using a modified Bridgman-type technique. Stoichiometric quantities of high purity antimony shots (purity 99.999%) and amorphous selenium shots (purity 99.999%) were loaded into cleaned and dried quartz ampoules. The mixture was repeatedly purged and eventually sealed under 1/3 argon atmosphere. These tubes were sealed in a second evacuated quartz ampoule and placed in a furnace at  $850^\circ\text{C}$  with a heating rate of  $180^\circ\text{C}/\text{h}$ . The temperature was held constant until the Se vapor disappeared, which occurred 3 days later. Then the mixtures were slowly cooled to  $450^\circ\text{C}$  within 100 h and kept at this temperature for 3 days. The quartz ampoules were eventually quenched to room temperature in air. The crystal structure and phase purity were verified by x-ray diffraction measurements on a STOE STADI P diffractometer with  $\text{Mo K}\alpha$  radiation (see Fig. SM1 of the Supplemental Material [19]). The crystals were further cut to obtain samples of few mm in size.

With the exception of AFM images, for which both cleavage and image acquisition occurred at ambient pressure, the so-obtained samples were cleaved with scotch tape in ultra-high vacuum (UHV) at pressures below  $1 \times 10^{-9}$  mbar and immediately analyzed. Cleavages were reproducible and very effective: the superficial layer could be completely removed from the sample, as can be seen by comparing the  $\text{Sb}_2\text{Se}_3$  samples before cleavage and the  $\text{Sb}_2\text{Se}_3$  residuals on the scotch tape after cleavage [Figs. 1(b) and 1(c)].

Measurements were performed with the sample at room temperature in a multi-technique UHV system based on a user-modified vacuum generator ESCALAB 220 [20], in a separate UHV system equipped with an Omicron variable-temperature STM, and using a Park Scientific Instruments designed Autoprobe CP-type AFM. XPS and XPD measurements were realized with a non-monochromatized  $\text{Mg K}\alpha$  x-ray source, providing photons with an energy of  $h\nu = 1253.6 \text{ eV}$ . XPD patterns were obtained by probing the photoemission intensity distribution of the  $\text{Sb } 3d_{5/2}$  and  $\text{Se } 3d_{5/2}$  core levels as a function of the emission angles at constant kinetic energy of the electrons after the subtraction of the inelastic background [21,22]. Data were recorded from grazing to normal emission, with the center of the plot corresponding to normal and the circumference to grazing emission. To account for the lower emission intensity parallel to the surface, a Gaussian-shaped polar background profile was subtracted from each pattern. The LEED electron gun used for this experiment is intentionally mounted off-center with respect to the sample holder. Thus, by rotating the sample in its azimuthal plane, it is possible to measure LEED patterns from different areas of the same surface. A monochromatized He-discharge lamp ( $\text{He } I_\alpha$ ,  $h\nu = 21.2 \text{ eV}$ ) was used for ARPES measurements [23] and for determining the work function  $\Phi = 4.55 \text{ eV}$ . In the latter case, the position of the valence-band secondary cutoff was measured while applying a negative bias to the sample (see Fig. SM2 for further details [19]).

For quantitative analysis of XPS spectra, curve fitting was performed by using Voigt functions after subtracting a Shirley-type background, and the binding energy (BE) scale was calibrated by measuring the  $\text{Au } 4f_{7/2}$  BE position of a freshly prepared  $\text{Au}(111)$  crystal ( $84.0 \text{ eV}$ , [24]). The adventitious carbon thickness was evaluated by using  $\text{C } 1s$  and  $\text{Sb } 3d$  peak intensities, neglecting the inelastic attenuation of the substrate emission, according to the formula shown in Ref. [22]. It amounted to about 20% of a monolayer of graphitic carbon. The BE scale for  $\text{He } I_\alpha$  measurements was calibrated considering the position of the Fermi edge on a cleaned polycrystalline silver sample. The STM scanner was calibrated by using the well-defined hexagonal boron nitride nanomesh superstructure on  $\text{Rh}(111)$  [25]. Surface lattice vectors were determined from LEED and STM data, with errors evaluated on a statistical basis, considering the values obtained from different LEED patterns and from Fourier transforms of several STM images. All the errors indicated on XPS results come directly from fitting analysis standard deviations or have been evaluated from standard deviations through error propagation.

## III. COMPUTATIONAL DETAILS

Simulations of  $\text{Sb } 3d_{5/2}$  and  $\text{Se } 3d_{5/2}$  XPD patterns were obtained by means of the *Electron Diffraction in Atomic Clusters* (EDAC) software [26]. For these simulations, an atomic cluster was prepared that represents the bulk structure truncated along a (100) plane.

ARPES data have been simulated for the unrelaxed bulk structure by using the crystalline structure obtained from the American Mineralogist Crystal Structure Database [27]. The first-principles calculations were carried out based on

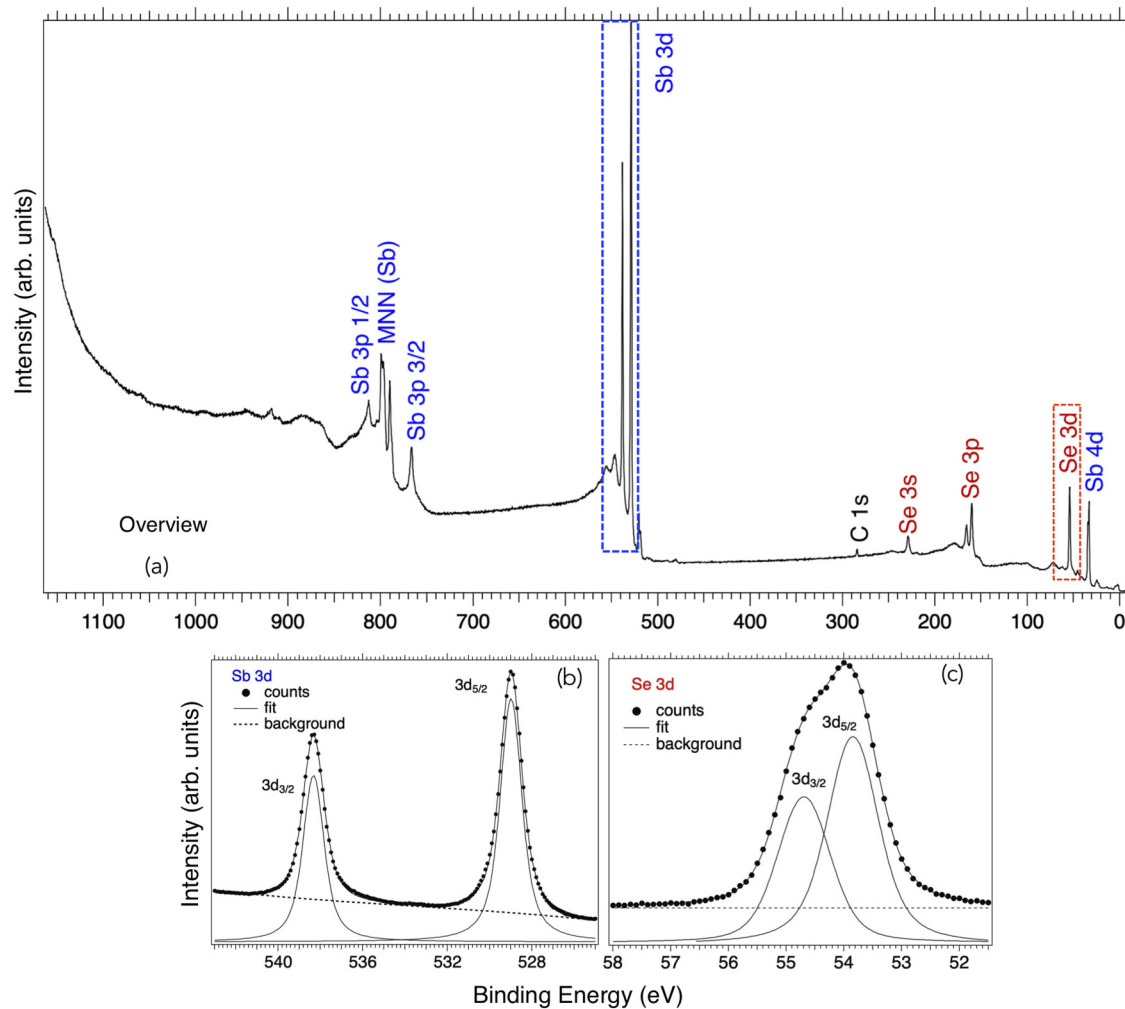


FIG. 2. XPS results,  $h\nu = 1253.6$  eV (non-monochromatized Mg  $K\alpha$  x-ray source): (a) Overview of UHV-cleaved Sb<sub>2</sub>Se<sub>3</sub>, (b) Sb 3d peaks and (c) Se 3d peaks with fitting analysis.

the density-functional theory (DFT) as implemented in the Vienna *ab initio* Simulation Package (VASP) [28,29], by using the projector augmented wave (PAW) method [30,31]. The generalized gradient approximation (GGA) with Perdew-Burke-Ernzerhof (PBE) realization [32] was adapted for the exchange-correlation potential. The plane-wave cutoff energy was set to 450 eV. The  $\Gamma$ -centered  $k$ -point mesh of size  $6 \times 20 \times 7$  was used for the Brillouin-zone sampling. The spin-orbit coupling effect was included in our calculations.

#### IV. RESULTS AND DISCUSSION

In Fig. 2, XPS results from a freshly cleaved Sb<sub>2</sub>Se<sub>3</sub> surface are shown. The overview spectrum [Fig. 2(a)] is dominated by Sb and Se core-level peaks and Sb MNN Auger peaks. There is a weak C 1s signal due to adventitious carbon, which we quantify as the equivalent of 0.23 monolayers of carbon coverage. Excluding the presence of oxygen was not that immediate because the typical O 1s BE region between 529 and 534 eV [24] overlaps with the strong Sb 3d<sub>5/2</sub> peak [Fig. 2(b)]. However, in this region, no evident features due to Sb<sub>2</sub>O<sub>3</sub> or molecular oxygen on the surface can be noticed on the Sb 3d<sub>5/2</sub> high BE tail, as was observed in previous works

[14,33]. Moreover, the Sb 3d peaks [Fig. 2(b)] could be fitted with just two components, consistent with the 3d<sub>5/2</sub> and 3d<sub>3/2</sub> spin-orbit doublet and centered at  $(528.99 \pm 0.01)$  eV and  $(538.33 \pm 0.01)$  eV, respectively. Both the energy splitting and area ratio (Table I) are very close to theoretical values [24], leaving no space for other peaks underneath the Sb 3d<sub>5/2</sub> experimental curve. As further proof of the absence of oxygen contamination, the most intense O KLL Auger peak is not detectable at 745 eV in the overview spectrum. Analogously to Sb 3d, the Se 3d spectrum [Fig. 2(c)] could be reproduced with a two-component fit, with peaks centered at  $(53.86 \pm 0.01)$  eV (3d<sub>5/2</sub>) and  $(54.7 \pm 0.01)$  eV (3d<sub>3/2</sub>). Also, in this case, the spin-orbit splitting and area ratio (Table I) are in good agreement with theoretical values [24]. The Sb and Se peak positions agree with BE values expected for Sb<sub>2</sub>Se<sub>3</sub> [14,34] and the ratio between Se 3d and Sb 3d total peak areas, divided by the respective cross sections and analyzer transmission function, matches the stoichiometric value of 1.5 (see Table I). All these results indicate a successful cleavage in UHV and a high quality and phase purity of our Sb<sub>2</sub>Se<sub>3</sub> single crystals.

The LEED pattern in Fig. 3(b), obtained with primary electron energy  $E_p = 35$  eV, shows a rectangular unit cell,

TABLE I. Binding energies for Sb 3*d* and Se 3*d* peaks, spin-orbit splitting ( $\Delta$ BE) and area ratio ( $X 3d_{5/2}/X 3d_{3/2}$ , where X = Sb, Se) and stoichiometry check via the ratio between Se 3*d* and Sb 3*d* total areas, divided by the respective cross sections and analyzer transmission function.

	Sb 3 <i>d</i> <sub>5/2</sub>	Sb 3 <i>d</i> <sub>3/2</sub>	Se 3 <i>d</i> <sub>5/2</sub>	Se 3 <i>d</i> <sub>3/2</sub>
BE (eV)	528.99 ± 0.01	538.33 ± 0.01	53.86 ± 0.1	54.72 ± 0.01
$\Delta$ BE (eV)		9.340 ± 0.014		0.860 ± 0.014
Spin-orbit doublets area ratio		1.512 ± 0.002		1.49 ± 0.05
$[A_{\text{Se}3d}/(\sigma_{\text{Se}3d} \cdot c_{\text{Se}3d})]/[A_{\text{Sb}3d}/(\sigma_{\text{Sb}3d} \cdot c_{\text{Sb}3d})]$				1.48 ± 0.02

defined by reciprocal lattice vectors  $\mathbf{a}_1^*$  and  $\mathbf{a}_2^*$ . The real lattice dimensions amount to  $a_1 = (11.2 \pm 0.5) \text{ \AA}$  and  $a_2 = (3.8 \pm 0.1) \text{ \AA}$ . Comparing them with the bulk crystalline structure (Table II), a good agreement is found by aligning the surface unit cell across two infinitely long 1D ribbons in the (100) plane, as shown in Fig. 3(a). In this way, we could establish the surface orientation as (100) which, as expected, corresponds to the predicted crystal cleavage planes plotted in Fig. 1(a).

A closer inspection of the LEED pattern shows a doubling of diffraction spots along the [010] direction. Moreover, when different areas on the same as-cleaved sample were probed, keeping  $E_p = 35 \text{ eV}$ , we obtained doublets [Figs. 3(b) and 3(d)], triplets [Fig. 3(e)], as well as single spots [Fig. 3(f)] and bright streaks [Fig. 3(c)]. Since the [010] direction is the ribbon direction, these results suggest a surface morphology characterized by structures with very different dimensions, interrupting the ideally infinite extension of the ribbons.

AFM images as shown in Fig. 4(a) indeed revealed the presence of parallel domains of unequal widths. Moreover, as shown by the height profile in Fig. 4(b), traced along the light-blue line in Fig. 4(a), these domains can be flat or slightly tilted with different angles of the order of a few tenths of a degree with respect to the horizontal direction. In gradually higher magnification images, STM characterization resolved the internal structure of the domains revealing parallel lines perpendicular to the domain boundaries [Figs. 4(c) and 4(d)]. In Figs. 4(e) and 4(f), high-resolution images of these features

are displayed. The Fourier transform of Fig. 4(f) is shown in Fig. 4(g). It reveals periodicities very similar to the LEED pattern, where the shorter periodicity (longer in real space) originates from the inter-ribbon periodicity, and the longer one (shorter in real space) from the Sb-Sb and Se-Se interatomic separation along the ribbons. Since lattice-parameter values from the STM Fourier transform,  $a_1 = (11.5 \pm 0.1) \text{ \AA}$  and  $a_2 = (4.1 \pm 0.1) \text{ \AA}$ , are also in good agreement with those obtained from the LEED analysis and with the corresponding numbers in the bulk crystalline structure (Table II), we were able to identify the parallel lines shown in STM images as the distinctive  $\text{Sb}_2\text{Se}_3$  1D ribbons along the [010] direction. Furthermore, the height modulation along the ribbon ridges of Fig. 4(f) can be associated with the Sb and Se internal arrangement inside the ribbons, as suggested by the higher spatial frequency along this direction in the STM Fourier transform shown in Fig. 4(g). We therefore conclude that domains of Fig. 4(a) are perpendicular to the ribbons and we propose that their misalignment with respect to the horizontal plane and their random widths produce the extra features observed in LEED patterns. Note that the orientations of the tilted domains were also previously calculated from the LEED patterns of Fig. 3(d). They turned out to be an order of magnitude higher ( $2^\circ$ – $3^\circ$ ). The resolution in the LEED patterns would not allow us to distinguish the extra diffraction features originating from domains tilted by only  $0.3^\circ$ . However, one has to consider that LEED probes macroscopic areas, while STM and AFM images cover much smaller areas that are typically selected

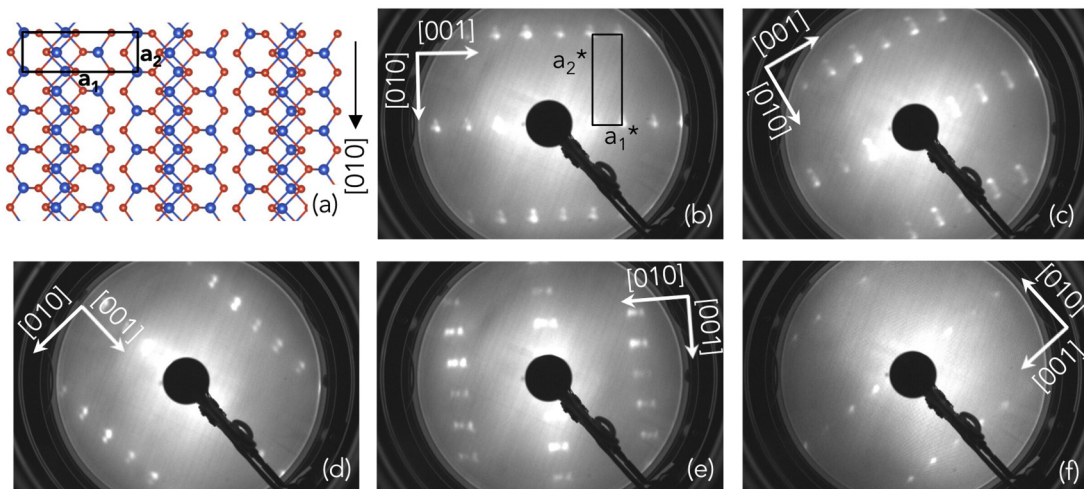


FIG. 3. (a) Schematic representation of extended 1D ribbons along the [010] direction; (b)–(f) LEED patterns ( $E_p = 35 \text{ eV}$ ) on different areas of the same  $\text{Sb}_2\text{Se}_3$  sample. In panel (b), the reciprocal-lattice unit cell, located by vectors  $\mathbf{a}_1^*$  and  $\mathbf{a}_2^*$ , is also indicated.

TABLE II. Summary of lattice constants obtained through different methods.

	$a_1$ (Å)	$a_2$ (Å)
FFT (STM)	$11.5 \pm 0.1$	$4.1 \pm 0.1$
LEED	$11.2 \pm 0.5$	$3.8 \pm 0.1$
Bulk Cryst. Struct.	11.7	4.0

based on reasonable imaging conditions. This would account for the higher angular value extracted from LEED results. The Fourier transform [Fig. 4(g)] of the obtained STM image does not show any splitting of spots because the image was taken on a single domain.

The origin of these peculiar domains remains speculative: the layered crystalline structure of Sb<sub>2</sub>Se<sub>3</sub> formed by 1D ribbons appears to be predisposed for accommodating this distinct morphology, as it was found repeatedly on various cleavings. It should be considered that cleavage is a rather brutal process when viewed at the atomic level. Our observation suggests that the material releases stress occurring during the separation of two adjacent crystal planes by gliding of crystal domains along ribbons rather than across, which may explain why the domain boundaries are invariably oriented perpendicular to the ribbons. This hypothesis seems to be confirmed by the fact that the difference in height between two adjacent domains matches the thickness of a Sb<sub>4</sub>Se<sub>6</sub> unit or multiples of it (see SM4 [19]). In any case, this morphology is remarkable, and it is a strong sign of strongly anisotropic friction forces within the cleavage planes.

From high-resolution STM images, we can also notice how 1D ribbons bestow the anisotropic bulk crystalline structure onto the surface under investigation, which assumes an equally pronounced anisotropic character.

The crystal orientation of the cleaved Sb<sub>2</sub>Se<sub>3</sub> surface was further confirmed by XPD data (Fig. 6). This is an angle-resolved XPS technique, probing the diffraction pattern produced by photoelectrons emitted from an element-specific core level after being scattered by neighboring atoms. The resulting angular intensity distribution is highly anisotropic and directly reflects the local crystalline structure around the emitting atom [21,22]. Sb 3d<sub>5/2</sub> and Se 3d<sub>5/2</sub> XPD patterns are displayed in Figs. 5(a) and 5(c): the local geometrical arrangement of both atoms exhibits a two-fold symmetry. In both patterns we recognize the influence of the 1D anisotropic structure seen also by STM: a bright streak along the [001] direction and a dark streak along the [010] direction. The bright streak is a consequence of strong forward scattering by the high number of coplanar atoms within the [Sb<sub>4</sub>Se<sub>6</sub>] units, i.e., within the (010) planes (Fig. 1). Figures 5(b) and 5(d) show EDAC simulations of Sb 3d<sub>5/2</sub> and Se 3d<sub>5/2</sub> XPD patterns, respectively. The good agreement between experiment and simulations in most of the fine features confirms the (100) orientation of the cleaved Sb<sub>2</sub>Se<sub>3</sub> surface and its unreconstructed nature. The presence of slightly tilted domains as found in the LEED and AFM data was not accounted for in the simulations. They would account for a smearing of the experimental XPD data along the [010] direction, which is not observed. This might be due to the different sampling of diffraction features in LEED (long-range periodicity) and in XPD (short-range atomic structure) that

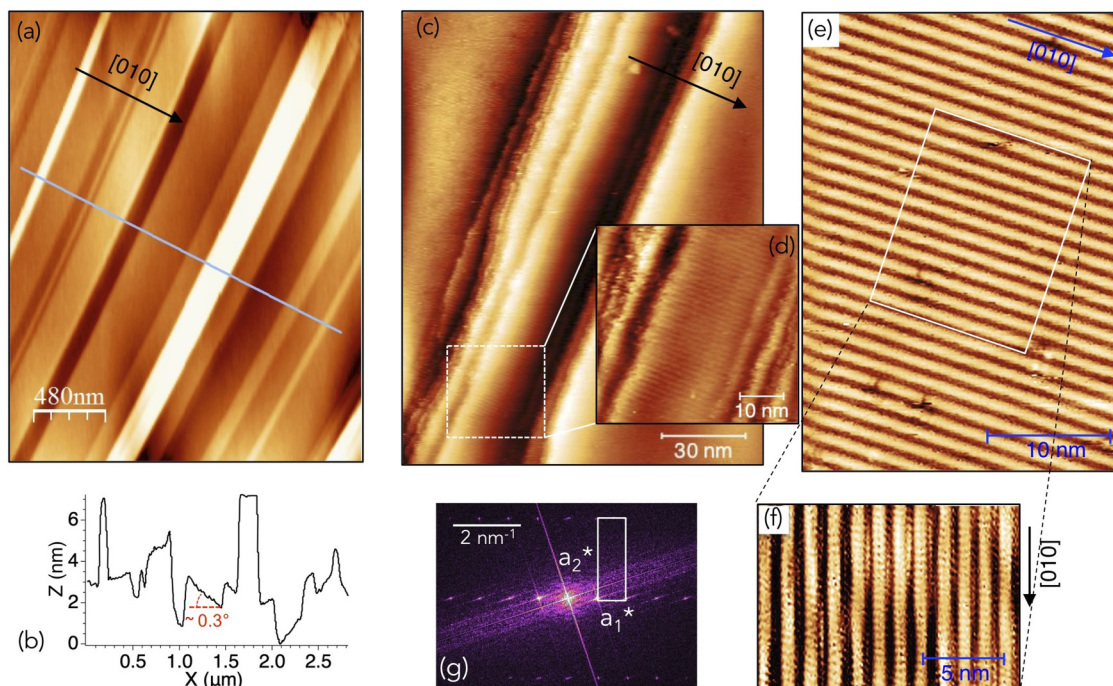


FIG. 4. (a) Contact-mode AFM image of Sb<sub>2</sub>Se<sub>3</sub>; (b) profile extracted along the light-blue line traced in panel (a). The steepest domain inclination is indicated. STM images at gradually higher magnifications showing (c) domains, (d) a 1D ribbons arrangement within domains, (e) high-resolution image of ribbons, and (f) their inner structure. (g) Fourier transform extracted from panel (f). STM images conditions: (c), (d)  $V_{\text{sample}} = 1.5$  V,  $I_{\text{tunnel}} = 150$  pA; (e), (f)  $V_{\text{sample}} = 1.2$  V,  $I_{\text{tunnel}} = 200$  pA.

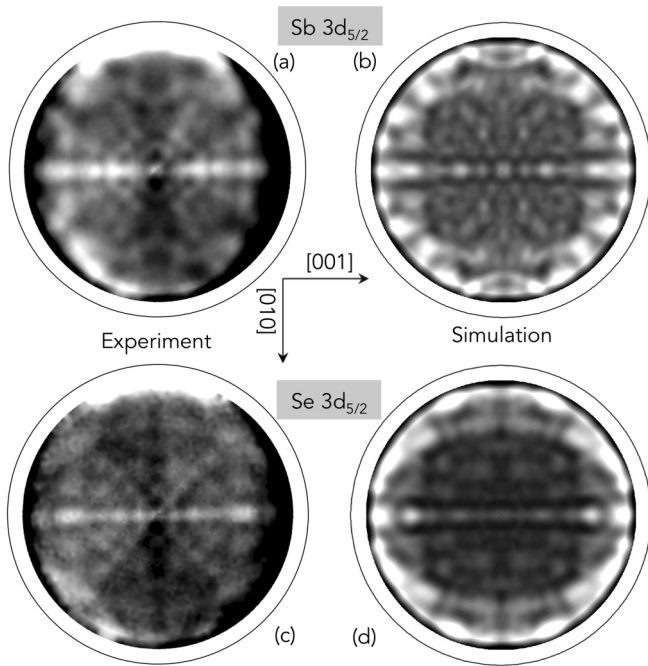


FIG. 5. XPD data ( $h\nu = 1253.6$  eV, non-monochromatized Mg  $K\alpha$  x-ray source) for (a) Sb  $3d_{5/2}$  and (c) Se  $3d_{5/2}$  core levels and (b), (d) corresponding multiple scattering cluster simulations performed with the EDAC software [26].

might tend to overemphasize the larger domains in the LEED data.

UV-excited photoemission was exploited to probe the band structure of the material. The valence-band maximum was measured at 0.56 eV of binding energy [see Fig. SM2(b)]. Figure 6(a) shows the obtained ARPES data along the  $\Gamma Y$  and  $\Gamma Z$  high-symmetry azimuths of the Brillouin zone [Fig. 6(c)], corresponding to the [010] and [001] directions of real space, respectively. Considering the values of real lattice parameters [11], we calculated the dimensions of the Brillouin zone to be  $a' = 0.533 \text{ \AA}^{-1}$ ,  $b' = 1.576 \text{ \AA}^{-1}$ , and  $c' = 0.539 \text{ \AA}^{-1}$ , thus  $\Gamma Z = c'/2 = 0.270 \text{ \AA}^{-1}$  and  $\Gamma Y = b'/2 = 0.788 \text{ \AA}^{-1}$ , which are in good agreement with the  $\Gamma Z$  and  $\Gamma Y$  values obtained from the first inflection points of the bands away from the surface normal, as observed in the ARPES data. Note that the data were taken with constant photon energy, which means that momenta are probed along a circular path in reciprocal space. The momentum axis in Fig. 6(a) refers to the momentum component parallel to the surface.

The anisotropy of the material is reflected in the measured band structure. The bands show a short periodicity in reciprocal space along the [001] ( $\Gamma Z$ ) direction, i.e., across the ribbons, and a longer periodicity along the [010] ( $\Gamma Y$ ) direction along the ribbons. The larger bandwidth and stronger band dispersion along  $\Gamma Y$  direction indicate that the electrons are less localized and have higher mobility along the chains. This is consistent with the presence of covalent bonds in

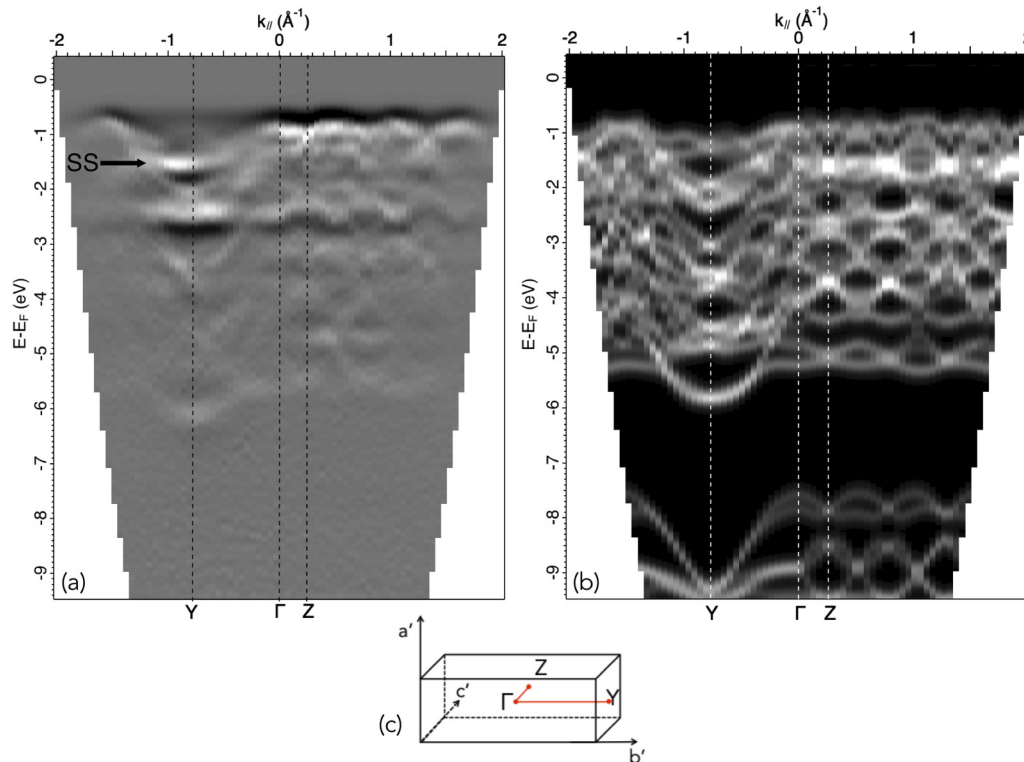


FIG. 6. Band structure of  $Sb_2Se_3$  surface obtained from (a) ARPES measurements ( $h\nu = 21.22$  eV, He  $I\alpha$ ) and (b) DFT calculations along the two perpendicular high-symmetry azimuths  $\Gamma Y$  (along ribbons) and  $\Gamma Z$  (across ribbons) of the (c) Brillouin zone. The ARPES measurements in panel (a) are presented as second derivative with respect to the energy coordinate. The black arrow indicates the putative surface state (SS) observed in the experimental data. A detailed explanation about the procedure followed to obtain DFT results at constant photon energy can be found in the SM section [19].

[Sb<sub>4</sub>Se<sub>6</sub>]<sub>n</sub> units inside ribbons and of only van der Waals interactions across adjacent ribbons.

The DFT calculations in Fig. 6(b) were carried out along the same circular paths that were measured [23], using free-electron final states and including also the refraction effects at the surface potential step, allowing a one-to-one comparison with the ARPES data.

The obtained theoretical results reproduce all the main experimental features visible down to ~6 eV below the Fermi level with a rather good agreement and resolve the numerous and intricate bands. There is one exception: a prominent band near the Y point with a BE of 1.5 eV in the ARPES data, indicated by a black arrow in Fig. 6(a), does not appear in the DFT results, suggesting that it is due to a surface state (SS). Interestingly, the bands in the higher BE region beyond 7.5 eV are completely missing in the ARPES data. Presumably, they are severely broadened by strong self-energy effects and consequently hidden under the secondary electron tail.

## V. CONCLUSIONS

Single crystals of Sb<sub>2</sub>Se<sub>3</sub> were cleaved and investigated by means of surface-science techniques. The high quality of the crystals, already proven by XRD data, was confirmed by XPS results, showing clean Sb and Se core level peaks, the correct stoichiometry of the crystal, and the absence of any other element except for a quarter monolayer of carbon. LEED analysis turned out to be a particularly insightful technique. In fact it was fundamental in determining the crystal orientation as (100), confirming that the studied surface corresponded to the expected crystal cleavage plane with ribbons of [Sb<sub>4</sub>Se<sub>6</sub>]<sub>n</sub> units running along the surface. STM images furnished a clear visualization of these ribbons and an initial demonstration that the Sb<sub>2</sub>Se<sub>3</sub> bulk anisotropy, due to the 1D crystal structure, is reflected on its surface. The observation of extra diffraction features along the ribbon direction in the LEED data motivated us to characterize the morphology of cleaved Sb<sub>2</sub>Se<sub>3</sub>(100) surfaces. With the additional support of AFM and STM images, we were able to identify the presence of unidirectional surface domains with domain boundaries oriented perpendicular to the ribbons. In these domains, the crystal lattice is either parallel or slightly tilted relative to the

average surface plane, with various tilt angles in the range of plus or minus a few degrees, but invariably oriented along the ribbons. We speculate that their appearance is related to the cleavage process, and that this observation suggests a pronounced anisotropy also in the friction forces along and perpendicular to the ribbons.

XPD data further confirm the surface orientation and reflect the twofold local geometrical arrangement around Sb and Se atoms. Importantly, fingerprints of the surface anisotropy were also recorded in XPD signal modulations from both Sb and Se core levels, producing two distinct features in XPD diffraction patterns. The band structure has been investigated by ARPES measurements with the support of DFT calculations. The probed momentum scans within the two high-symmetry azimuths, containing the [010] and [001] directions in the real space, reflect the structural anisotropy by showing different periodicities and bandwidths. Moreover, our data suggest the presence of a surface state near the Brillouin zone boundary along the ribbon direction, with a BE of about 1.5 eV. Considering the growing importance of Sb<sub>2</sub>Se<sub>3</sub> in photocatalysis, this surface characterization will allow a more rational design of complex heterostructures such as used in photovoltaic and photoelectrochemical cells. Furthermore, it is a solid starting point for deeper investigations in more realistic conditions, i.e., in an aqueous environment and at (near) ambient pressure, to shed light on the reasons behind Sb<sub>2</sub>Se<sub>3</sub> high stability against photocorrosion.

## ACKNOWLEDGMENTS

The authors are grateful to Gabriele de Luca and Marta Gibert for assistance during AFM measurements, to Lara Pestrin for help with the synthesis of the samples, and to Matthias Hengsberger for fruitful discussions. J.-Z.Z. acknowledges the Pauli Center for funding his visit at the University of Zürich. This project was financed under the University Research Priority Program LightChEC of the University of Zürich. F.O.v.R. acknowledges financial support from the Swiss National Science Foundation under Grant No. PZ00P2\_174015 and the Ernst Göhner Fellowship 2019 awarded by the “Fond zur Förderung des akademischen Nachwuchts” (FAN).

- 
- [1] H. Zhang, C.-X. Liu, X.-L. Qi, X. Dai, Z. Fang, and S.-C. Zhang, *Nat. Phys.* **5**, 438 (2009).
  - [2] S. D. Shutov, V. V. Sobolev, Y. V. Popov, and S. N. Shestatskii, *Phys. Status Solidi* **31**, K23 (1969).
  - [3] Z. Hurych, D. Davis, D. Buczek, C. Wood, G. J. Lapeyre, and A. D. Baer, *Phys. Rev. B* **9**, 4392 (1974).
  - [4] J. Black, E. M. Conwell, L. Seigle, and C. W. Spencer, *J. Phys. Chem. Solids* **2**, 240 (1957).
  - [5] F. D. Rosi, B. Abeles, and R. V. Jensen, *J. Phys. Chem. Solids* **10**, 191 (1959).
  - [6] G. J. Snyder and E. S. Toberer, *Nat. Mater.* **7**, 105 (2008).
  - [7] N. S. Platakis and H. C. Gatos, *Phys. Status Solidi A* **13**, K1 (1972).
  - [8] P. Arun, A. G. Vedeshwar, and N. C. Mehra, *J. Phys. D: Appl. Phys.* **32**, 183 (1999).
  - [9] Y. Zhou, M. Leng, Z. Xia, J. Zhong, H. Song, X. Liu, B. Yang, J. Zhang, J. Chen, K. Zhou, J. Han, Y. Cheng, and J. Tang, *Adv. Energy Mater.* **4**, 1301846 (2014).
  - [10] S. Chen, A. Walsh, X.-G. Gong, and S.-H. Wei, *Adv. Mater.* **25**, 1522 (2013).
  - [11] R. Vadapoo, S. Krishnan, H. Yilmaz, and Carlos Marin, *Phys. Status Solidi B* **248**, 700 (2011).
  - [12] Y. Zhou, L. Wang, S. Chen, S. Qin, X. Liu, J. Chen, D.-J. Xue, M. Luo, Y. Cao, Y. Cheng, E. H. Sargent, and J. Tang, *Nat. Photonics* **9**, 409 (2015).
  - [13] K. Zeng, D.-J. Xue, and J. Tang, *Semicond. Sci. Technol.* **31**, 063001 (2016).

- [14] X. Liu, J. Chen, M. Luo, M. Leng, Z. Xia, Y. Zhou, S. Qin, D.-J. Xue, L. Lv, H. Huang, D. Niu, and J. Tang, *ACS Appl. Mater. Interfaces*, **6**, 10687 (2014).
- [15] J. Kim, W. Yang, Y. Oh, H. Lee, S. Lee, H. Shin, J. Kim, and J. Moon, *J. Mater. Chem. A* **5**, 2180 (2017).
- [16] W. Yang, J. Ahn, Y. Oh, J. Tan, H. Lee, J. Park, H.-C. Kwon, J. Kim, W. Jo, J. Kim, and J. Moon, *Adv. Energy Mater.* **8**, 1702888 (2018).
- [17] L. Zhang, Y. Li, C. Li, Q. Chen, Z. Zhen, X. Jiang, M. Zhong, F. Zhang, and H. Zhu, *ACS Nano* **11**, 12753 (2017).
- [18] N. W. Tideswell, F. H. Kruse, and J. D. McCullough, *Acta Crystallogr.* **10**, 99 (1957).
- [19] See Supplemental Material at <http://link.aps.org/supplemental/10.1103/PhysRevMaterials.3.125404> for XRD data, VB onset, and secondary cutoff for work function evaluation, ARPES raw data, large-area STM images with corresponding line profiles along ribbon direction, and detailed explanation about DFT for ARPES at constant photon energy.
- [20] T. Greber, O. Raetz, T. J. Kreutz, P. Schwaller, W. Deichmann, E. Wetli, and J. Osterwalder, *Rev. Sci. Instrum.* **68**, 4549 (1997).
- [21] C. S. Fadley, in *Synchrotron Radiation Research: Advances in Surface Science*, edited by R. Z. Bachrach (Plenum, New York, 1990), Chap. 11.
- [22] J. Osterwalder, in *Surface Analysis by Auger and X-Ray Photoelectron Spectroscopy*, edited by D. Briggs and J. T. Grant (IM Publications, Chichester, and Surface Spectra Limited, Manchester, 2003), Chap. 20.
- [23] J. Osterwalder, *Surf. Rev. Lett.* **4**, 391 (1997).
- [24] J. F. Moulder, W. F. Stickle, P. E. Sobol, and K. D. Bomben, *Handbook of Photoelectron Spectroscopy*, edited by Chastain (Perkin-Elmer Corporation, Eden Prairie, 1992).
- [25] M. Corso, W. Auwärter, M. Muntwiler, A. Tamai, T. Greber, and J. Osterwalder, *Science* **303**, 217 (2004).
- [26] F. J. Garcia de Abajo, M. A. Van Hove, and C. S. Fadley, *Phys. Rev. B* **63**, 075404 (2001).
- [27] <http://rruff.geo.arizona.edu/AMS/minerals/Antimonselite>.
- [28] G. Kresse and J. Furthmüller, *Phys. Rev. B* **54**, 11169 (1996).
- [29] G. Kresse and J. Furthmüller, *Comput. Mater. Sci.* **6**, 15 (1996).
- [30] G. Kresse and D. Joubert, *Phys. Rev. B* **59**, 1758 (1999).
- [31] P. E. Blöchl, *Phys. Rev. B* **50**, 17953 (1994).
- [32] J. P. Perdew, K. Burke, and M. Ernzerhof, *Phys. Rev. Lett.* **77**, 3865 (1996).
- [33] R. R. Prabhakar, W. Septina, S. Siol, T. Moehl, R. Wick-Joliat, and S. D. Tilley, *J. Mater. Chem. A* **5**, 23139 (2017).
- [34] R. Browning, N. Kuperman, B. Moon, and R. Solanki, *Electronics* **6**, 27 (2017).